LAWRENCE
LIVERMORE
NATIONAL
LABORATORY

UCRL-TR-202345

# Modeling and characterization of recompressed damaged materials

*R. Becker, J.U. Cazamias, D.H. Kalantar*
*M.M. LeBlanc,and H.K. Springer*

**February 13, 2004**

**Disclaimer**

This document was prepared as an account of work sponsored by an agency of the United States Government. Neither the United States Government nor the University of California nor any of their employees, makes any warranty, express or implied, or assumes any legal liability or responsibility for the accuracy, completeness, or usefulness of any information, apparatus, product, or process disclosed, or represents that its use would not infringe privately owned rights. Reference herein to any specific commercial product, process, or service by trade name, trademark, manufacturer, or otherwise, does not necessarily constitute or imply its endorsement, recommendation, or favoring by the United States Government or the University of California. The views and opinions of authors expressed herein do not necessarily state or reflect those of the United States Government or the University of California, and shall not be used for advertising or product endorsement purposes.

This work was performed under the auspices of the U.S. Department of Energy by University of California, Lawrence Livermore National Laboratory under Contract W-7405-Eng-48.

This research is funded by the Laboratory Directed Research and Development (LDRD) Program at Lawrence Livermore National Laboratory (LLNL) under project 01-ERD-032. The LDRD Program is mandated by Congress to fund laboratory-initiated, long-term research and development (R&D) projects in support of the DOE and national laboratories' mission areas. The Director's Office LDRD Program at LLNL funds creative and innovative R&D to ensure the scientific vitality of the Laboratory in mission-related scientific disciplines.

# Modeling and Characterization of Recompressed Damaged Materials

**Summary report for LDRD 01-ERD-032**

R. Becker, J.U. Cazamias, D.H. Kalantar, M.M. LeBlanc and H.K.Springer

University of California, Lawrence Livermore National Laboratory, Livermore, CA, 94550

## Abstract

Experiments have been performed to explore conditions under which spall damage is recompressed with the ultimate goal of developing a predictive model. Spall is introduced through traditional gas gun techniques or with laser ablation. Recompression techniques producing a uniaxial stress state, such as a Hopkinson bar, do not create sufficient confinement to close the porosity. Higher stress triaxialities achieved through a gas gun or laser recompression can close the spall. Characterization of the recompressed samples by optical metallography and electron microscopy reveal a narrow, highly deformed process zone. At the higher pressures achieved in the gas gun, little evidence of spall remains other than differentially etched features in the optical micrographs. With the very high strain rates achieved with laser techniques there is jetting from voids and other signs of turbulent metal flow. Simulations of spall and recompression on micromechanical models containing a single void suggest that it might be possible to represent the recompression using models similar to those employed for void growth. Calculations using multiple, randomly distributed voids are needed to determine if such models will yield the proper behavior for more realistic microstructures.

## 1 Introduction

Materials subjected to dynamic loading from high velocity impacts, explosive loading or laser ablation frequently incur internal damage in the form of spall. Spall in metals is caused by nucleation and growth of voids under tensile loading conditions created by the interaction of stress waves with surfaces and interfaces. When a compressive shock wave reflects off of a surface it creates a tensile wave with approximately the same stress magnitude. If the tensile stress is sufficiently high, voids can nucleate around particles or defects in the material and grow. Spall and the resulting damage have been studied extensively for shock loading created by gas guns (Thissell, et al, 2000), explosives (Gray, et al, 2003) and laser ablation (Budil, et al, 2001).

In dynamic loading situations the material continues to deform after spall occurs, and numerical simulations must be able to track the deformation reliably. Hence, it is important that material models not only predict spall, but they must also capture the post-spall material response. The particular post-spall deformation of interest here is closure of the spall by continued loading. This situation arises for explosively driven metals when the material that is being pushed directly by the explosive catches up to and impacts the spalled layer. Recompression of spall can also occur when spalled materials impact other structures, as in debris shields or layered armor. Unfortunately, little work has been done to characterize spalled materials subjected to recompression. The behavior of the recompressed interface is expected to exhibit some properties of explosively welded interfaces (Brasher and Butler, 1995) and shock compacted materials (Meyers, et al., 1999). Some research has been done to examine the bonding mechanisms for these processes (Plaksin, et al., 2003).

The goal of this work is to develop experimental methods to explore the behavior of recompressed spall and to provide data illustrating the conditions under which full recompression of the spall will occur. As the work is exploratory in nature, various approaches are used and the data collected establishes a basis for further investigations. The modeling component of this study is aimed at understanding the behavior of spall-related voids when subjected to recompression. Characterization of the stresses involved in void collapse is a critical component in constructing continuum level models of post-spall behavior.

## 2 Experimental Procedure

Experiments aimed at determining conditions under which spall recompression could be induced were conducted on high purity copper at a variety of pressures and strain rates. Spall was introduced through either gas gun or laser techniques with soft capture procedures to recover the targets with minimal additional deformation. Some of the gas gun targets were machined into compression specimens to be further deformed quasi-statically or in a split-Hopkinson bar. Others were subjected to recompression immediately following spall with the compressive stress induced by a second disk placed in the flyer package. The laser recompression tests were all performed on recovered samples with laser-induced spall damage.

### *2.1 Gas gun experiments*

The gas gun experiments were run on a 35 mm light gas gun. The targets spalled for further experimentation on recovered specimens were 5.0 mm thick and 16.5 mm diameter. The design includes additional momentum trap rings to mitigate the effects of radial relief waves, Figure 1. The flyer plate was a 3.0 mm thick aluminum disk abutted to a polycarbonate sabot. Flyer velocities of 65, 120 and 150 m/s were used to produce samples with a range of spall damage. The targets were soft-captured and sectioned along a diameter for characterization of the spall damage

by optical metallography. A 3-D simulation of the experiment depicting the separation of the momentum trap rings following impact is shown in Figure 2. The Gurson ductile damage model was used to simulate the copper target and the contours show accumulated damage.

The targets for experiments with recompression immediately following spall were thinner so that the recompression would occur before a significant portion of the specimen was affected by the radial relief waves. The target thickness chosen for these experiments was 4.0 mm. The flyer thickness was reduced to 2.7 mm to keep the spall plane roughly centered through the thickness of the target. The flyer package included a 1.3 mm thick polycarbonate layer adjacent to the flyer followed by a 3.0 mm thick tantalum disk to provide the recompression pulse, Figure 3. The pressure rise induced by the sandwiched polycarbonate disk occurs over a significantly longer time period than would be the case for two impacting flyers, so the recompression pulse has a relatively long rise time. This set of experiments also included controls run at the same velocities but without the tantalum disk in the flyer package. The spall damage in these samples should be the same as the former, but they are not subjected to recompression. The copper stock used for these samples was in a half-hard condition. This condition is different that the fully annealed copper used in the 5.0 mm specimens described earlier. Results from a simulation used to determine this design are given in Figure 4. Figure 4a shows contours of longitudinal stress responsible for the spall and Figure 4b shows the compressive stress induced later by the additional tantalum flyer. The majority of the target diameter experiences a significant recompression stress.

Velocimetry was used on all of the gas gun experiments to provide a free surface velocity profile at a temporal resolution of 0.1 microseconds. The technique involves the use of a thin mirror that is shattered as the specimen proceeds down the target chamber. The target then passes through a 20.0 mm diameter steel stripper tube to remove the momentum trap rings. The center portion of the target is then captured in a cylinder filled with 0.??? g/cc foam.

*2.2 Further experiments on recovered gas gun samples*

Following metallography on the 5.0 mm thick recovered targets, four 4.32 mm diameter compression specimens were excised from the center 11.5 mm of each 16.5 mm disk. Given the three different flyer velocities, this resulted in three sets of four similarly damaged samples. These smaller cylinders were compressed 15% in a quasi-static load frame at a strain rate of 0.01 $sec^{-1}$ and in a split-Hopkinson bar at strain rates of 2000 and 4500 $sec^{-1}$. Duplicate compression tests were run at the highest strain rate. The tests provided a range of recompression conditions on the same spall-damaged microstructure.

Following compression, the duplicate samples from the high rate compression tests were sectioned to assess the change in spall damage. The three remaining recompressed cylinders at each damage level were machined into miniature tensile specimens approximately 4 mm long and with a 1.5 mm diameter. The specimen design and the specialized loading fixture are shown in Figure 5. The specimens were pulled to failure in a standard load frame.

*2.3 Laser experiments*

Laser spall and recompression experiments were conducted on LLNL's JANUS laser facility. The specimens were polycrystalline copper. Deformation was induced by either direct laser ablation or ablation of a coating. The coating was used to minimize damage to the base material. The laser energies ranged from 85 J to 125 J, and the spot size was approximately 1 mm.

The experiments were conducted in two sessions. During the first session, two types of tests were preformed. One set of these tests utilized spalled samples acquired from previous, unrelated

experiments on 1.0 mm thick, 5.0 mm square specimens. Several of these specimens were sectioned and examined metallographically to assess the extent of the spall damage, Figure 6. This particular sample was shocked at 125 J. The indentation from the laser pulse is evident opposite the spall blister. The samples to be subjected to recompression had a ??? coating applied over the surface containing the existing spall blister, and they were recompressed by focusing the laser on the blister.

The second type of experiment in this first set involved coating new, 0.5 mm thick, 3.0 mm square samples. These were laser shocked to produce spalled specimens for use in the subsequent experimental session. Based on the recompression results with the acquired specimens, the laser energy was reduced to limit the size of the blister. It is suspected that significant laser energy went into collapsing the blister, leaving less energy available for recompression of the spalled material.

The 0.5 mm thick copper targets spalled in the first series of tests were subsequently coated on the side opposite the initial laser strike in preparation for the second round of experiments. Experiments during the second session consisted of recompression by focusing the laser on the existing spall blister.

## 3 Results

### *3.1 Gas gun spall*

Free surface velocity measurements from the three 5.0 mm thick gas gun targets are shown in Figure 7. A spall signature is evident for the 120 and 150 m/s flyer velocities, but not the 65 m/s shot.

The recovered targets were sectioned across a diameter and examined using optical metallography to determine the extent of the spall damage. The experiment with the 65 m/s impact velocity did not exhibit visible damage, as expected. Micrographs of both halves of the other two samples are shown in Figure 8. The 120 m/s shot shows significant damage by isolated voids along the spall plane. In the specimen from the 150 m/s experiment the voids along the spall plane are nearly interconnected.

The extent of damage was quantified by using high resolution, high contrast versions of the images shown in Figure 8. A slender rectangular box, 5 μm wide and extending along the spall plane, was stepped across the damaged region. The void fraction within the box was determined by obtaining the percentage of black pixels in the box. The resulting void distributions are shown in Figure 9 for both halves of the two incipiently spalled specimens. Since the spall planes are not straight, the measurement window sampled regions at various relative locations with respect to the center of the damaged region. As a result, theses types of averaged measurements give a peak void fraction level significantly lower than appears locally in the micrographs.

The figures also appear to have secondary peaks to either side of the main void concentration. By examination of the micrographs, these could be due to the presence of discrete voids that may appear on either side of the primary damage location. The reduced stress field around growing voids creates an exclusion zone so that the secondary voids are separate.

### *3.2 Results from recompression of spalled gas gun targets*

The stress-strain curves for the 2000 $sec^{-1}$ recompression tests in the Hopkinson bar are shown in Figure 10. It is notable that the sample with the lowest damage level has the lowest flow strength, and the one with the greatest spall damage has the highest flow strength. Results for the quasi-static test and those at a strain rate of 4500 $sec^{-1}$ are similar. It is expected that the higher

strength for the samples with greater damage is a result of the stronger shock loading causing greater strain hardening. The strain hardening has a greater effect than the presence of the voids.

An optical micrograph of a specimen shocked at 150 m/s and recompressed 15% at 4500 $sec^{-1}$ is shown in Figure 11 along with a portion of the micrograph showing the initial spall damage. The porosity is not closed on recompression. Given the compressive displacement compared to the size of the voids, nonclosure of the voids is only possible if significant deformation occurred in the unvoided regions of the sample. Considering stress equilibrium, such a deformation pattern is indicative of significant strain hardening in the voided region. The high hardening is consistent with the ordering of the compression stress-strain curves as a function of shock loading, Figure 10. These results suggest that stress states with higher confining pressures are required to close the spall-induced porosity.

Stress-strain curves from the subscale tensile tests on the material recompressed at 4500 $sec^{-1}$ are given in Figure 12. Unlike the compression response, the tensile results are ordered with the most heavily damaged material having the lowest strength. In addition, the strain to failure is significantly reduced in the specimen with the greatest spall damage. Damage dominated the tensile response.

Fractography on the tensile specimens shows the spall-induced voids viewed from the normal to the spall plane, Figure 13a. Although the specimens were fabricated from high purity copper, examination of the voids reveals that sub-micron zirconium containing particles served as void nucleation sites, Figure 13b.

*3.3 Integrated spall and recompression specimens*

Gas gun experiments on the 4.0 mm thick copper specimens with a tantalum disk embedded in the flyer assembly were designed to achieve high pressure to close the spall-induced porosity. Control experiments without the tantalum disk reveal the extent of damage prior to recompression. Micrographs for the control samples run at 165 and 220 m/s are shown in Figure 14. A pattern of isolated voids is seen for the lower velocity, while the porosity is nearly fully connected for the higher impact velocity.

Optical micrographs of the spall plane at the same magnification are shown in Figures 15 and 16 for the experiments with flyers containing the tantalum disks. Both sets of micrographs exhibit a feature running across the image that is asserted to be the remnant of the spall damage. The samples were heavily etched to ensure that voids were not smeared over during polishing. At the lower velocity, these features contain residual voids in support of this conclusion. Also for the 165 m/s shot, there are additional isolated voids above and below the feature. These are consistent with the off-plane voids evident in Figure 14a.

The transverse feature from the higher velocity shot, Figures 16, shows no obvious residual porosity. The feature appears in the same location on the sample thickness as does the spall on the control sample, and there is no evidence of the spall plane having existed anywhere else in the specimen. A high-resolution grain orientation map using an Electron Back Scatter Diffraction technique shows that this feature is comprised of small scale recrystallized grains, Figure 17. Such a microstructure is consistent with recrystallization of a localized, highly deformation zone, possible while at an elevated temperature. Such conditions would exist in a recompressed spall layer.

Free surface velocimetry from these experiments is shown in Figure 18. Results from the control and the recompression test are plotted on the same graphs to highlight the similarities and differences between the tests. In both cases, the control test is indicated by the blue curve, and the

red curve is the result with the tantalum disk inserted in the flyer. The velocity rise in the red curves at 4 and 3.2 us, for the low and high velocities respectively, results from the compression wave induced by the tantalum disk.

At the lower velocity, Figure 18a, the two tests had very similar initial loading profiles, and the velocity on the first pullback is nearly the same for both. However, the subsequent rise following this first pullback is significantly different. The blue curve shows a trough about as wide as the width of the initial loading pulse. This indicates that there was little stress relief from spall, in agreement with the low spall damage observed in Figure 14a. The red curve, on the other hand, has a valley width about half this size suggesting a new surface was created internally. This indicates significant spall damage. This seeming inconsistency can result from material and configuration variations when loading is near the incipient spall threshold. Some specimens will spall, some will not. It is also evident from Figure 14a that the spall is not uniform, and the free surface velocity could vary from location to location. The possible difference in initial spall damage between the control and the recompression tests should be born in mind when interpreting the 165 m/s results.

The velocity traces for the higher speed shot show greater similarity. This is to be expected when the loading is far from incipient spall conditions. Both curves show approximately the same minimum on the first pullback, and the subsequent rise and recoil are indicative of the stress pulse traversing the spalled layer. The recompression pulse enters shortly after 3 us. The rise is not nearly as steep as the initial loading pulse because the pressure driving the recompression builds up gradually in the polycarbonate layer between the aluminum flyer and the tantalum disk. At approximately 170 m/s the red curve deflects and then continues to rise at the previous rate. This feature is associated with recompression of the spall voids. It is possible that other features of the recompression curve can be associated with specific physical processes, but more data would be needed before drawing further conclusions.

*3.4 Laser processed samples*

Samples similar to the laser-spalled specimen shown in Figure 6 were subjected to recompression loading. It was recovered and examined with optical metallography. An example is shown in Figure 19. The residual porosity is evident at the left side of the micrograph. Further examination of the recompressed spall region was carried out at higher resolution using a scanning electron microscope (SEM), with the results given in Figure 20. Visible in this image are partially closed voids, regions of fine scale residual porosity and a highly deformed twin structure in the vicinity of the prior spall plane. At a higher SEM resolution the fine-scale porous region resembles foam, Figure 20b. Another interesting feature is a void that appears to be partially closed by a jetting mechanism, Figure 20c. Visible within this collapsed void is a particle that may have been the nucleation site for the void on initial spall.

An example of one of the spalled samples created during the first round of test is shown in Figure 21. The spall damage is evident; and, as desired, the blister is significantly smaller than for the samples shown in Figure 6. Recompression was run at high laser energy to ensure closure of the spall.

A typical result from the second set of laser recompression experiments is shown by the SEM micrographs in Figure 22. A macroscopic view of the sample is given in Figure 22a. The initial laser shot hit the specimen on the right side creating a spall dimple on the left. The recompression pulse hit the left side of the specimen, closing the spall blister and completely spalling off a piece on the right hand side. A higher magnification of the recompressed surface is given in Figure 22b. While there are a few voids present, it is not possible to discern conclusively where the spall plane

was. Examination of the twin structure reveals boundaries oriented horizontally near the surface. This indicates significant deformation and/or recrystallization near this surface. The opposite side of the specimen, Figure 22c, shows additional voids beneath the newly created spall surface.

All of the recompressed specimens from this second series of tests have a similar appearance. They were all overdriven to the point that no information can be obtained regarding mechanisms for closure of the spall porosity.

Only a qualitative assessment can be made for the laser results. There are several reasons for this with the most significant being that the correspondence between experimental conditions and the micrographs was lost for the first set of results. As the second series of tests did not produce discernable recompression information, complete data is not available for any of the interesting specimens. Also, the laser pulse was not characterized quantitatively for these experimental conditions. Finally, during the majority of the first shot series, a debris shield in the laser path showed signs that it was reflecting light, thus diverting some of the power. After this was removed, the remainder of the samples saw a higher loading for the same facility settings.

## 4 Micromechanical Modeling

Micromechanical modeling of a periodic void structure was performed in ALE3D to obtain a better understanding of the behavior of the voids during spall and recompression and to assess the importance of strain hardening.

### *4.1 Unit cell model description*

The model region is a one-eighth symmetry section of a 200 μm copper cube with an initial void fraction of $10^{-5}$, Figure 23. The finite element mesh contains a fine rectangular region near one corner, and the void is "shaped in" by assigning void properties to elements and fractions of elements that contain the small spherical void. The mesh is coarsened away from the initial void so the element sizes at opposite boundaries are quite large by comparison. The majority of the mesh is run in an Eulerian mode so that the fine resolution existing near the origin is retained. A strip of material near the loading surface is run in ALE mode to accommodate the moving boundary.

Symmetry conditions were applied to all surfaces except the loading surface. This creates a uniaxial strain state similar to what material experiences during spall. The loading surface is pulled at a constant velocity until the model has expanded 50% greater than its initial volume. Then the loading direction is reversed, recompressing the region to its initial volume. The deformation is performed approximately at a strain rate of $10^4$ $sec^{-1}$. This is a compromise between faster turn around time for higher strain rate simulations and a desire for a low strain rates to eliminate inertial effects. The goal is to capture effects of material strength and the void fraction independent of dynamic loading.

To assess the effects of strain hardening more easily, a power law hardening material was used. The yield strength was held constant at 120 MPa and the strain hardening exponent was changed from a very low value of 0.0001 to a moderate value of 0.2.

Stress was computed for the unit cell model by volume averages of the various stress components. The stress computed by summing forces over the planar faces was also tracked for comparison. Values from the two methods agree to within several percent throughout most of the analyses, but the measures of triaxiality (mean stress divided by the von Mises stress) diverge when the von Mises stress computed from face loading goes to zero near the end of the stretching portion

of the calculation. The volume averaging method did not exhibit this singularity, so all stresses reported are from volume averages.

*4.2 Unit cell model results*

The due to the low strain rate, small element size and large deformation, the simulations are quite lengthy, requiring on the $10^5$ or more time steps. To keep the computational requirements tractable, the meshes are coarse. The mesh coarseness is partially responsible for advection related mesh imprinting on the open void shape; sometimes the imprinting was severe. The effects were generally worse for the materials with higher strain hardening. Even though there are known errors in the void shape, it is felt that volume averaged results, such as the stress-strain response and void volume fraction, are not as sensitive to the configuration as are measures like void aspect ratio.

Void shapes at maximum extension and following recompression to the initial volume are shown in Figure 24 for strain hardening exponents of 0.0001 and 0.2. It is seen that strain hardening alters void shape. The shape differences in the distended plots are likely reasonable reflection of the hardening differences. The mesh related advection errors noted above might have affected the recompressed void shapes more significantly.

The absolute value of the applied stress is plotted against the logarithm of the void fraction in Figure 25. The curves correspond to the two different strain hardening behaviors described above. The deformation begins at a void fraction of $10^{-5}$ and zero stress. The blue, upper curve is for the material with higher strain hardening. The stress rises steeply with applied loading, and then the voids quickly snap open to a void fraction of approximately 0.01. Inertial effects from this snap result in a momentary stress drop followed by resumed loading and a gradual stress drop to zero as the voids continue to grow. The stress for the lower hardening material drops steadily at large void fractions while the slope for the higher hardening material tends to change at about 20% void fraction. The voids are coalesced and the applied stress is zero at the end of the extension phase of the loading.

The stress increase on recompression follows the terminal slope of the opening response. For the low hardening material the recompression curve follows the loading curve down to a void fraction of 0.01. The recompression response for the material with greater strain hardening is significantly higher than the opening response.

Many models of void growth are based on an equilibrium solution for a thick walled spherical shell in which the stress triaxiality is linearly related to the log of the void fraction (Torre, 1948; Rice and Tracey, 1969; Green 1972; Carroll and Holt, 1972). Stress triaxiality is plotted against the log of the void fraction in Figure 26 for unit cell models with several different strain hardening exponents. The tensile response is represented by the upper curves and the compressive response has a negative triaxiality. As with the response shown in Figure 25, the initial portion of the void growth is dynamic as the voids snap open. As the voids continue to grow, the stress triaxiality is nearly linear with the log of void fraction up to void fractions on the order of 0.1. Similarly, the compression response is also approximately linear between void fractions of 0.1 and 0.001. The curves for the lower strain hardening materials are nearly identical, and it is only for strain hardening exponents of 0.1 or greater that hardening affects the response noticeably.

These results provide a means for understanding fracture and recompression response. However, in unit cell simulations the voids close precisely on their symmetric halves. In a more realistic situation the surfaces on either side of the spall plane would likely experience a relative shift or the irregularity of the void pattern would break the symmetry. If the void parts are not

aligned, closure would begin at a lower void volume fraction and the stress rise would be sharper. These alignment effects are likely to change the response significantly.

*4.3 Gurson model comparison*

A single element simulation using the Gurson (1977) void growth model was subjected to the same loading conditions as the unit cell calculations. The response is given by the black curve in Figure 26 for comparison with the more detailed simulations. It can be seen that predictions from the Gurson model are fairly close throughout most of the loading history. The linear dependence is captured and the slope is approximately correct. Comparing with the results from the low hardening unit cell simulations, it is notable that the Gurson model falls below the detailed results on opening and also below on recompression. Since the curves from the Gurson model can be shifted up and down by adjusting the $q_1$ parameter (Tvergaard, 1981), it appears that the Gurson model can be used for both expansion and recompression. The $q_1$ parameter can be changed to reflect whether the deformation is tension or recompression. However, in light of the comments above about simulation errors due to not accounting for misalignment and multiple void effects, a more definitive statement about $q$ factors would need to be substantiated by simulations employing multiple voids.

## 5 Summary and Conclusions

Recovered gas gun spall specimens subjected to recompression either quasistatically or in a Hopkinson bar had significant residual porosity after 15% compression strain. The strain hardening in the vicinity of the voids countered the strength decrease due to the presence of the voids so that, after some straining in the vicinity of the voids, the net strength of the voided region was similar to the remainder of the sample. Since these particular recompression techniques produce an approximate uniaxial stress state, significant deformation occurred outside of the voided region. Hence, it is not possible to recompress porosity significantly in a high hardening material under a uniaxial stress state.

The higher confining stress achieved in a gas gun can drive total void collapse. A recompression pulse initiated by a secondary tantalum disk in the flyer package produced sufficient compressive stress to close the spall plane. The velocimetry trace from the recompression shot shows an inflection related to deformation during void closure. The remnants of the spall planes in micrographs of the recovered spalled and recompressed samples appear as differentially etched features. At the lower gas gun velocities small voids remain on the recompression feature, while at the higher flyer velocities no residual voids could be found.

Laser shocks also produce high confining pressures, and spall blisters can be driven closed. In one experiment with a large spall blister, significant laser energy was utilized in plastically deforming the blister and recompression was incomplete. In this case, recompression created fine scale porosity along the prior spall plane, and evidence of material jetting into voids was also observed. The laser energy applied in a series of recompression tests with small spall blisters was well in excess of that needed to close the voids, and no definitive indication of the prior spall planes could be found.

Unit cell simulations of void formation and recompression have been run to quantify the loading needed to drive the process. While the deformation process was in a uniaxial strain mode, the void growth response followed a trend expected for a void under pure triaxial tension; the stress triaxiality was linear with the log of the void fraction over a large portion of the deformation. The

response can be matched fairly well by the Gurson model provided that the $q_1$ parameter is different for void expansion and recompression. While these results are encouraging, the coalescence and recompression of multiple voids could involve more complicated interaction mechanisms. Additional simulations with multiple voids would be necessary to determine if the linear relationship holds for more realistic void distributions.

## 6 Recommendations for Future Work

Several areas for further investigation of spall recompression can be identified based on results of this exploratory research. Gas gun data at other velocities and with recompression flyers of other densities are needed to quantify the closure response. It would also be useful to use different drive mechanisms for the recompression, such as gap between the flyers rather than the polymer disk. This will change the reloading behavior. Creating a different spall pattern with graded density flyers would produce recompression data similar to what would be expected with a Taylor wave from explosive loading. A more complete characterization of the material is also needed. This could include quantification of residual porosity and mechanical testing on the recovered specimens to assess the strength of the closed spall.

The laser experiments show great promise to yield interesting results. However, unless the appropriate range of desired operating conditions are identified before a run of tests, it will be more productive to run the experiments in several short blocks of time than in one dedicated time slot. The breaks will permit metallographic examination of the specimens and appropriate adjustment of operating conditions. Once appropriate energies are identified for spall and recompression, these experiments can be combined into a single laser shot with a slight delay on the recompression beam.

While experimentation will give insight into mechanisms and provide critical validation data, it is not possible to directly obtain stress state information vital to model development. Detailed micromechanical models explicitly accounting for void growth and interactions among dozens of discrete voids would provide a tremendous boost to coarse scale model development efforts. The micromechanical models will enable characterization of material response as a function of void fraction, stress state and loading history. This information is essential for development of product-level models utilized in large-scale simulations.

**Acknowledgements**
The contributions to this effort by Chad Goerzen, Mukul Kumar, Kim Budil and Neal Hinsey are greatly appreciated. This work was performed under the auspices of the U.S. Department of Energy by University of California, Lawrence Livermore National Laboratory under Contract W-7405-Eng-48. Funding was provided through LDRD 01-ERD-032.

## References

Brasher, D.G. and Butler, D.J., 1995, “Explosive welding- principles and potentials,” Adv. Mater. Proc. V. 147, p. 37.

Budil, K.S., Ault, E.R., Shepp, T.A., Colvin, J.D., King, W.E., Zimmerman, Hackel, L., Kumar, M., Clauson, T., and Thoe, R., 2001, “Laser shock experiments investigating spall in metals,” Abstracts the Amer. Chem. Soc., V. 222.

Carroll, M.M. and Holt, A.C., 1972, “Static and dynamic pore-collapse relations for ductile porous materials,” J. Appl. Phys., Vol. 43, p. 1626.

Gray, G.T., Bourne, N.K. Henrie, B.L. and Millett, J.C.F, 2003, “Influence of shock-wave profile shape (triangular –‘Taylor-wave’ versus square-topped) on the spallation response of 316L stainless steel,” J. de Phys. IV, Vol. 10, p 773.

Gurson, A.L., 1977, “Continuum theory of ductile rupture by void nucleation and growth: Part I – yield criteria and flow rules for porous ductile media,” J. Engr. Mat. Tech., Vol. 99, p. 2.

Green, R.J., 1972, “A plasticity theory for porous solids,” Int. J. Mech. Sci., Vol. 14, p. 215.

Meyers, M.A., Benson, D.J. and Olevsky, E.A., 1999, “Shock consolidation: Microstructurally-based analysis and computation modeling,” Acta Mater, Vol. 47, p. 2089.

Plaksin, I., Campos, J., Ribeiro, J. Mendes, R., Direito, J., Braga, D. and Pruemmer, R., 2003, “Novelities in physics of explosive welding and powder compaction,” J. de Phys. VI, Vol. 110, p. 797.

Rice, J.R. and Tracey, D.M., 1969, “On the ductile enlargement of voids in triaxial stress fields,” J. Mech. Phys. Solids, Vol. 17, p. 201.

Thissell, W.R. Zurek, A.K. MacDougall, D.A.S. and Tonks, D., 2000, “Damage evolution and damage model validation in spalled tantalum,” J. de Phys. IV, Vol. 10P, p. 769.

Tvergaard, V., 1981, “Influence of voids on shear band instabilities under plane strain conditions,” Int. J. Fracture., Vol. 17, p. 389.

Torre, 1948, “Theorie and verhalten zusammengepresster pulver”, Berg-u hüttenmänn. Monatsh, Vol. 93, p. 62.

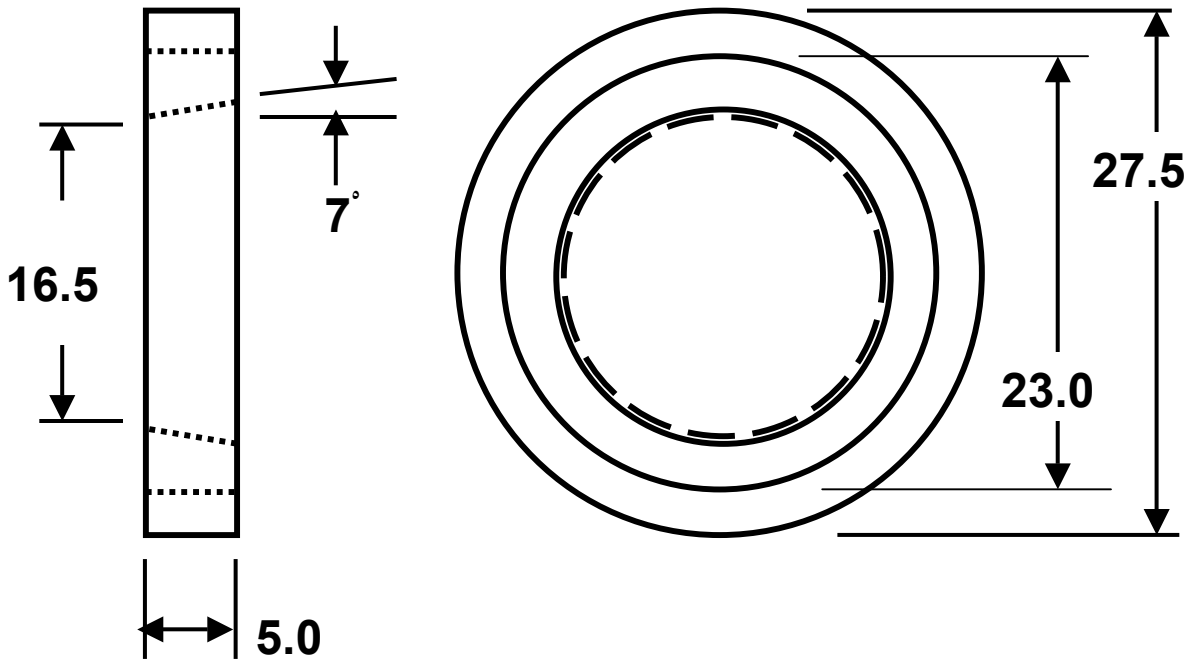


Figure 1. Gas gun target geometry. Dimensions are in mm.

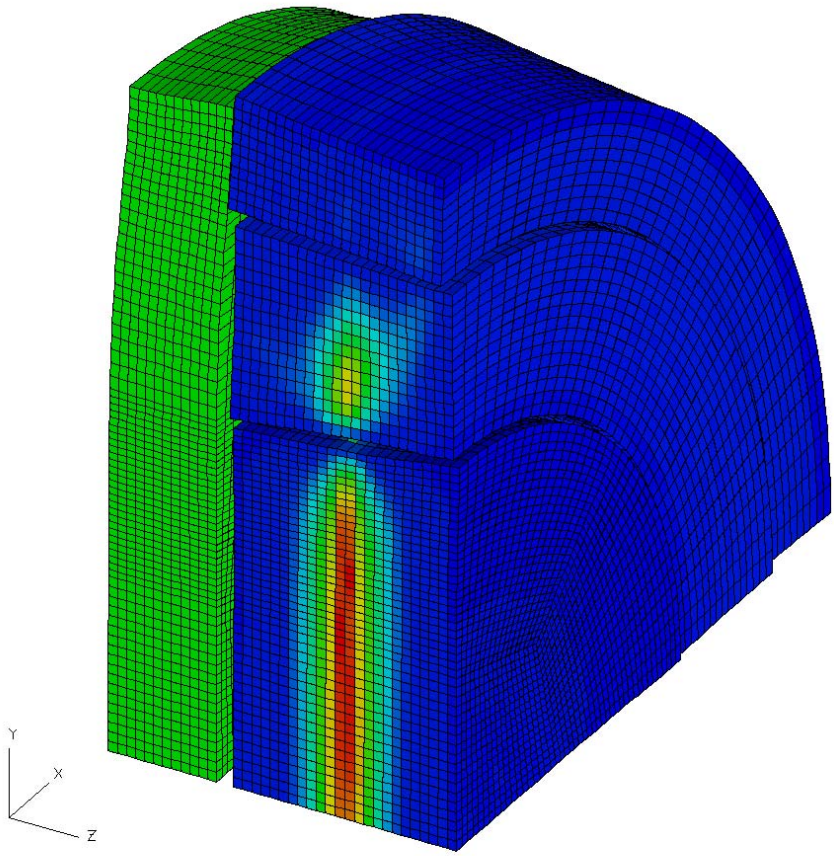


Figure 2. Simulation of the gas gun target following impact showing the separation of the momentum trap rings. The contours are of void fraction associated with the Gurson model.

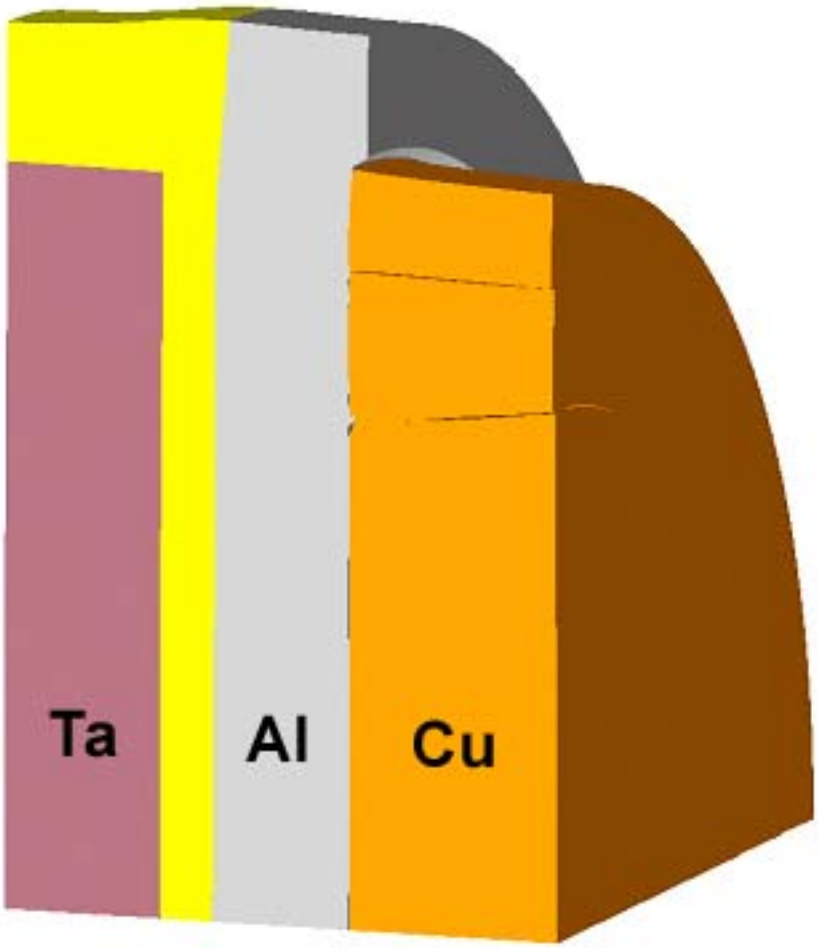


Figure 3. Target and flyer package for gas gun recompression experiments.

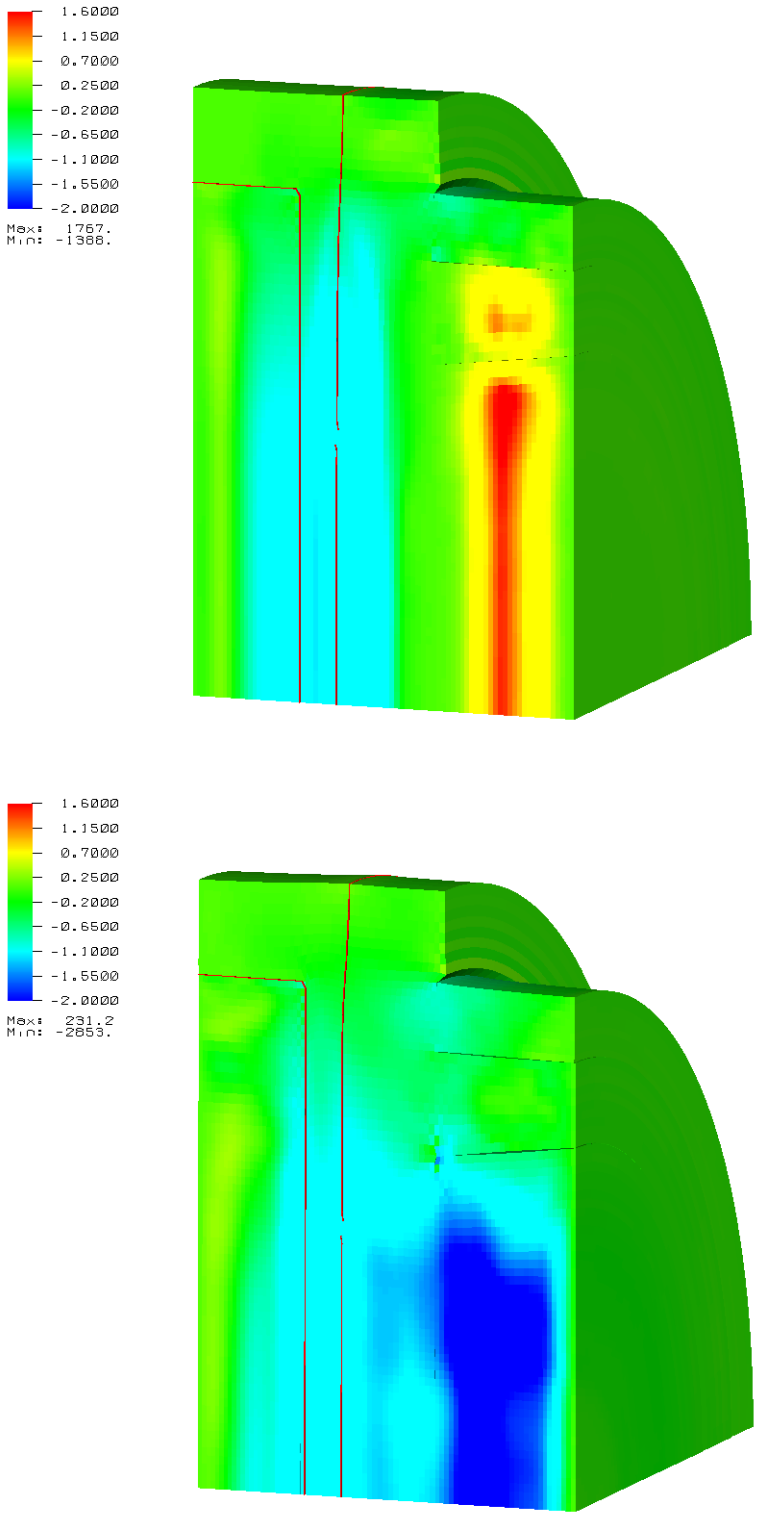


Figure 4. Contour plots showing calculated a) peak tensile stress and b) peak recompression stress for the gas gun recompression experiments

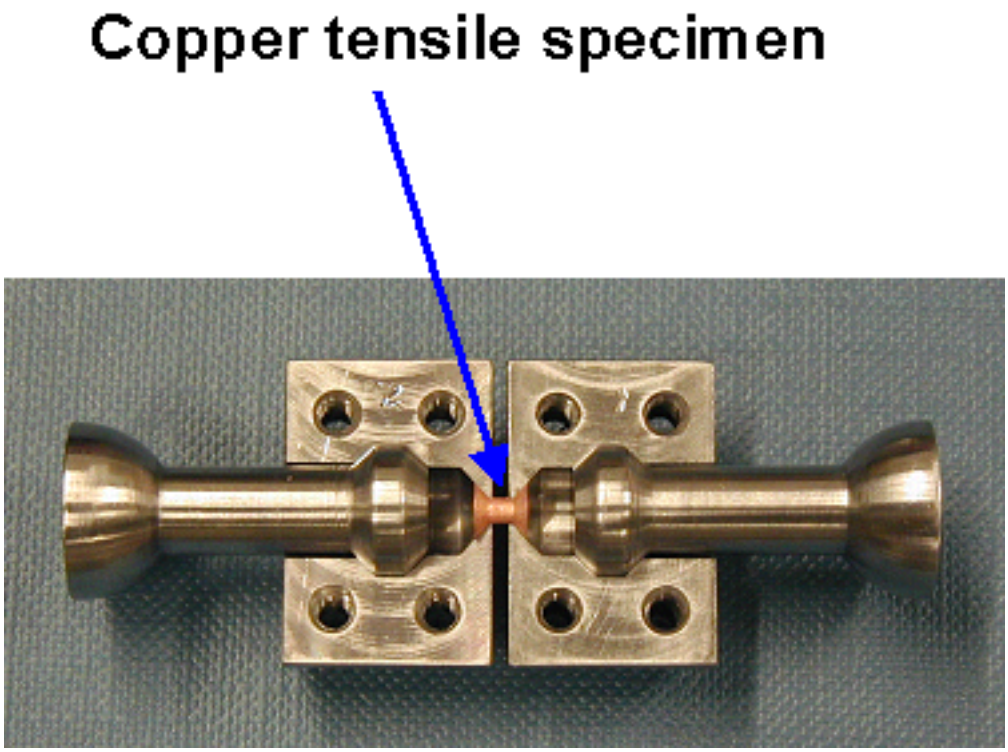


Figure 5.  Subscale copper tensile specimen in specialized grips

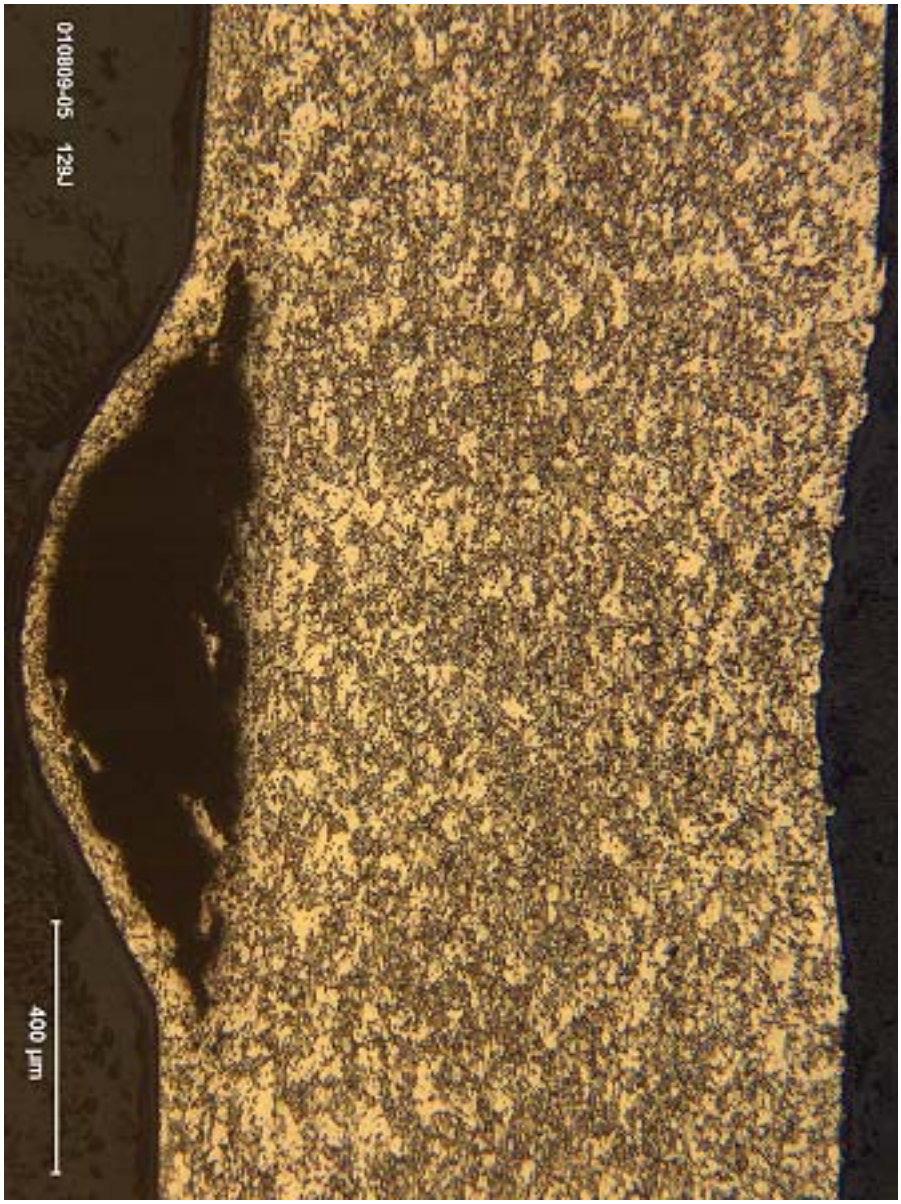


Figure 6. Laser spalled and recovered specimen similar to those used in first set of laser recompression experiments. The original thickness was 1.0 mm.

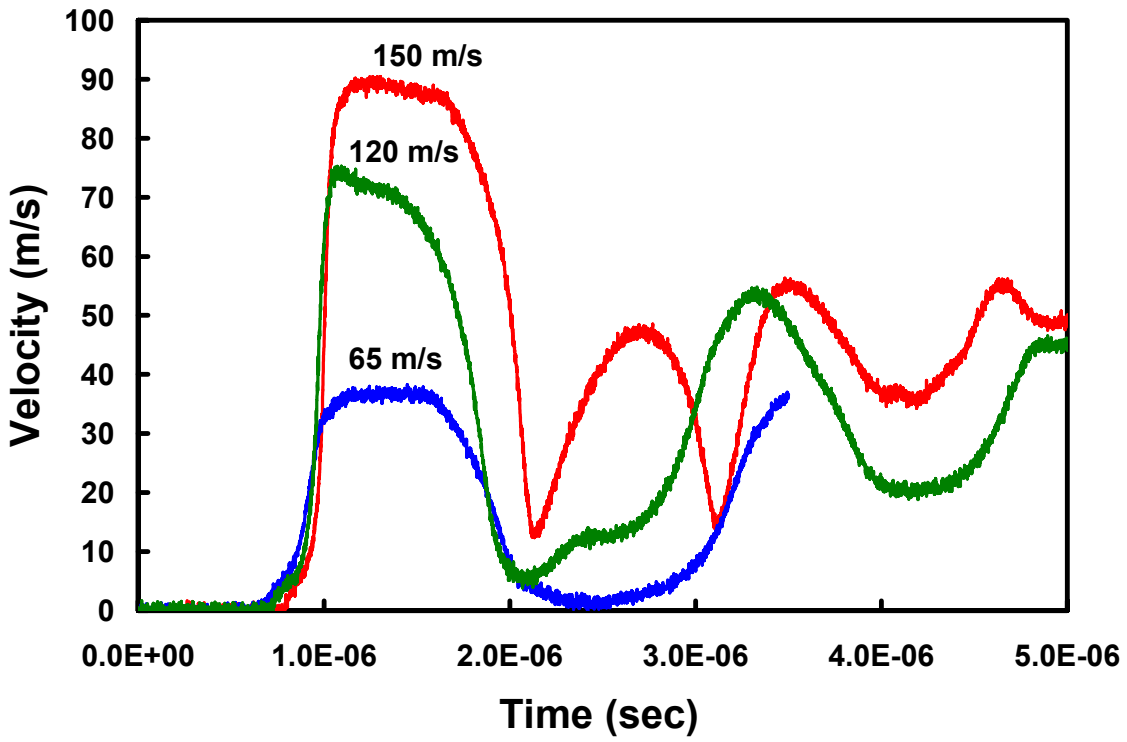


Figure 7. Free surface velocity measurement for 5.0 mm gas gun targets tested at flyer velocities of 150 (red), 120 (green) and 65 m/ s (blue).

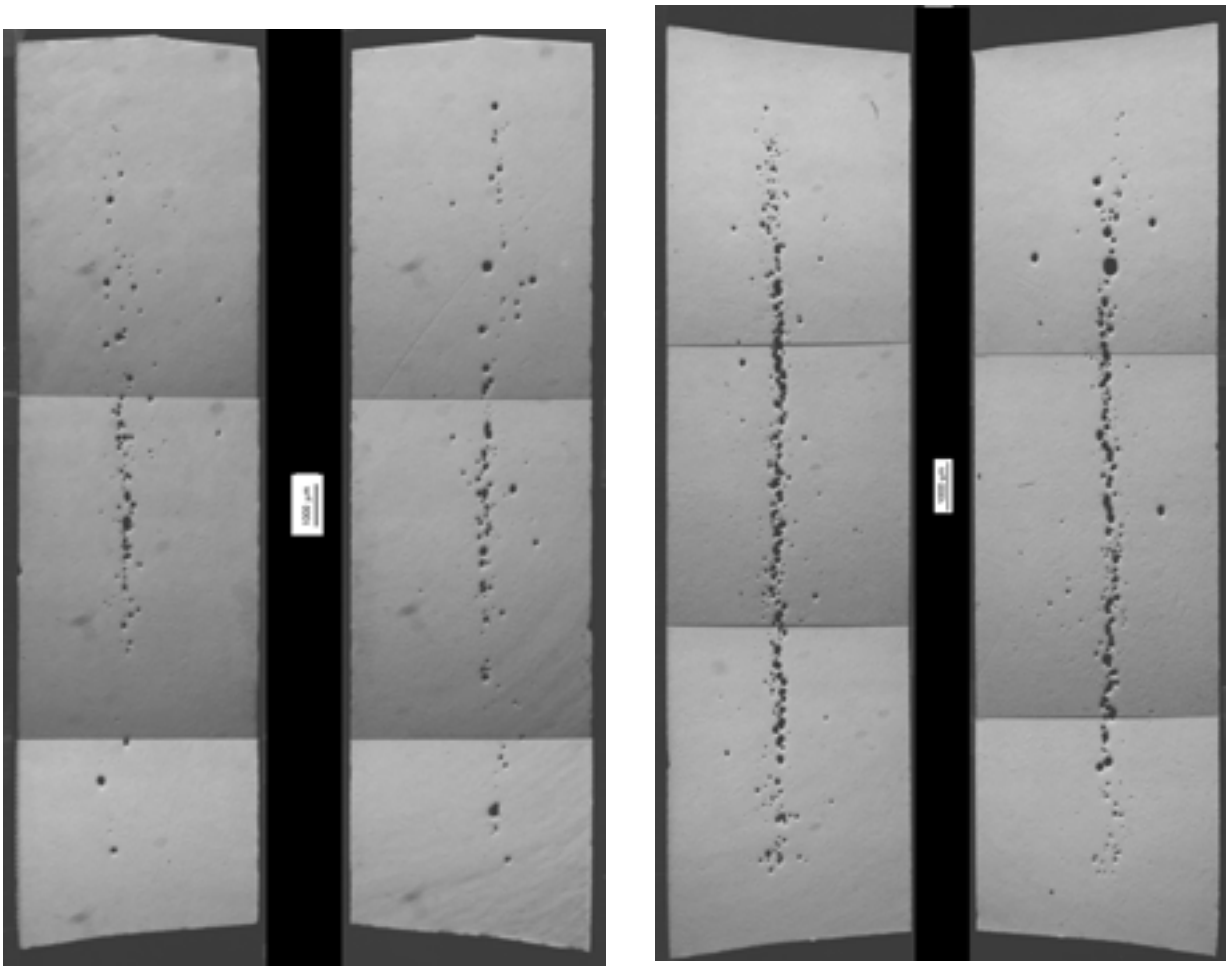

**120 m/s** **150 m/s**

Figure 8. Spall damage in 5.0 mm thick copper gas gun targets fired at 120 and 150 m/s.

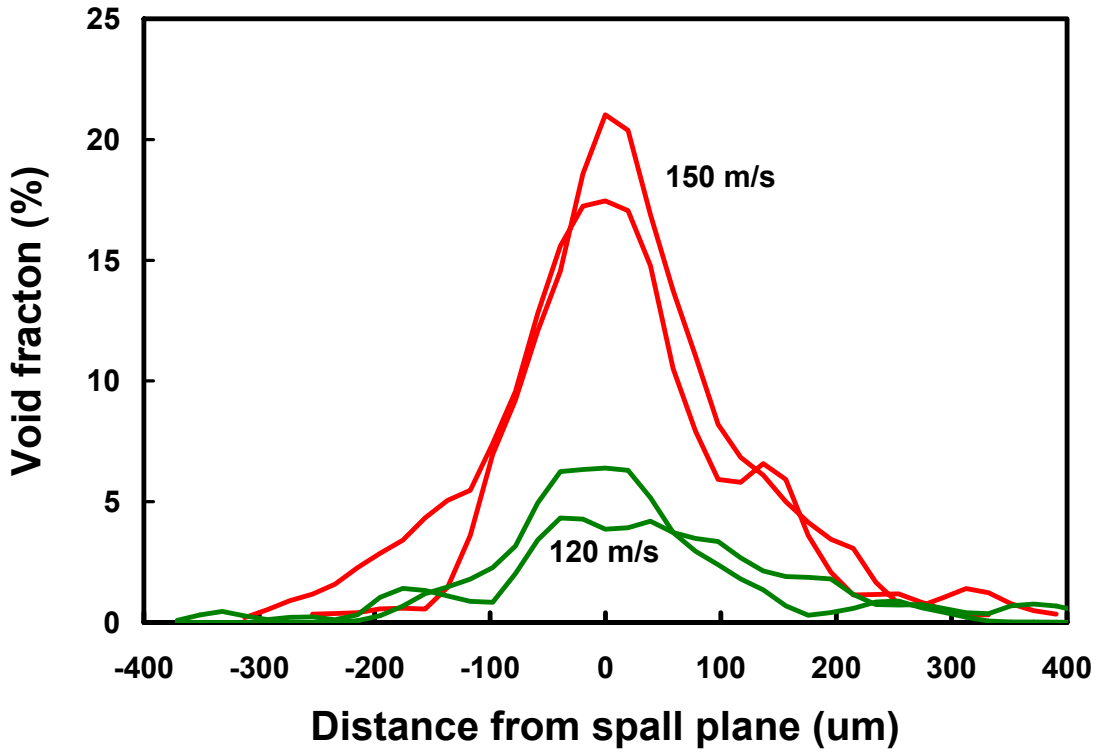


Figure 9. Average void fraction measured across the spall plane for the specimens in Figure 8

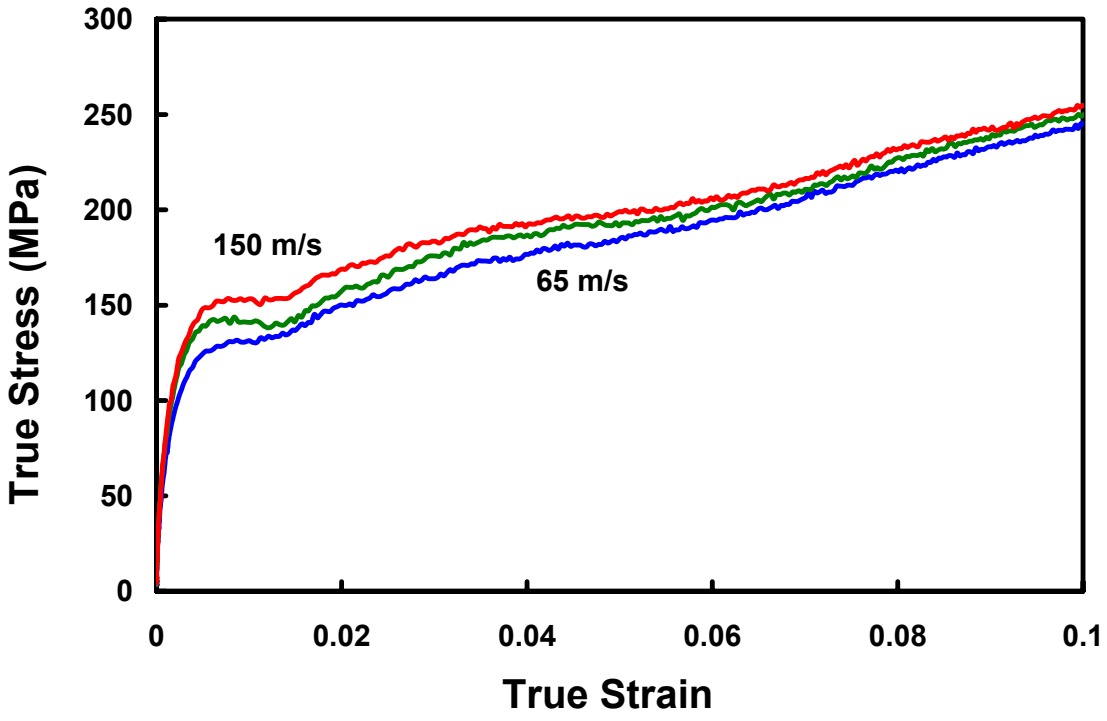


Figure 10. Stress-strain curves for recompression in a Hopkinson bar at strain rate 2000 $sec^{-1}$

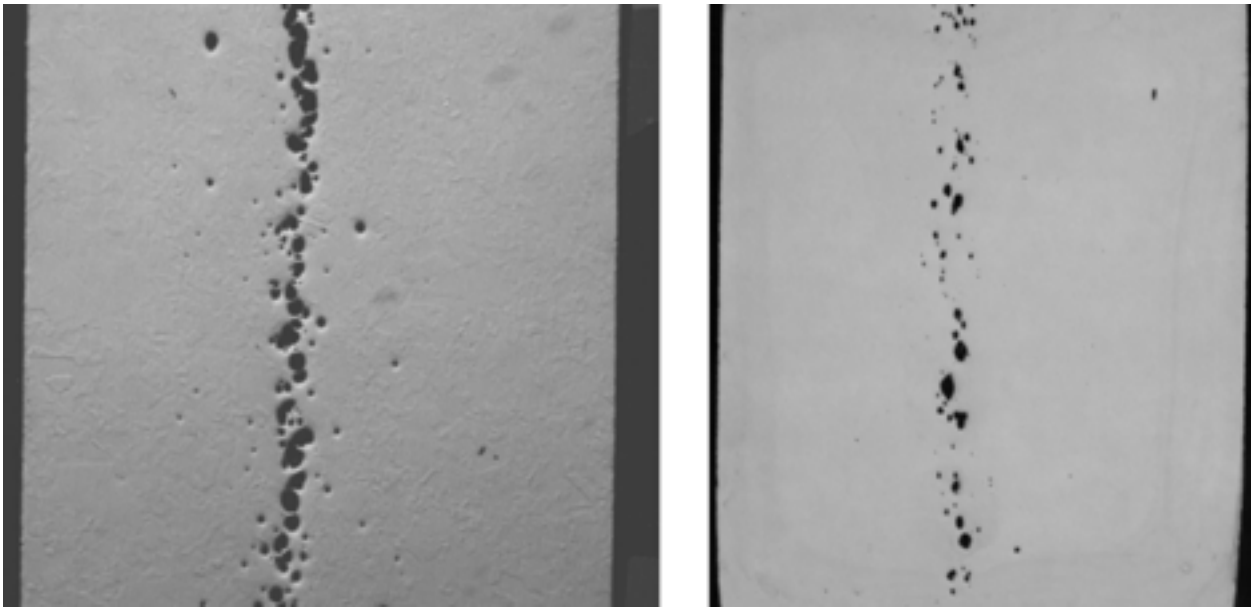

**as-spalled** **recompressed**

Figure 11. Comparison of voids in the as-spalled sample and following 15% recompression in a Hopkinson bar at a strain rate of 4500 $sec^{-1}$.

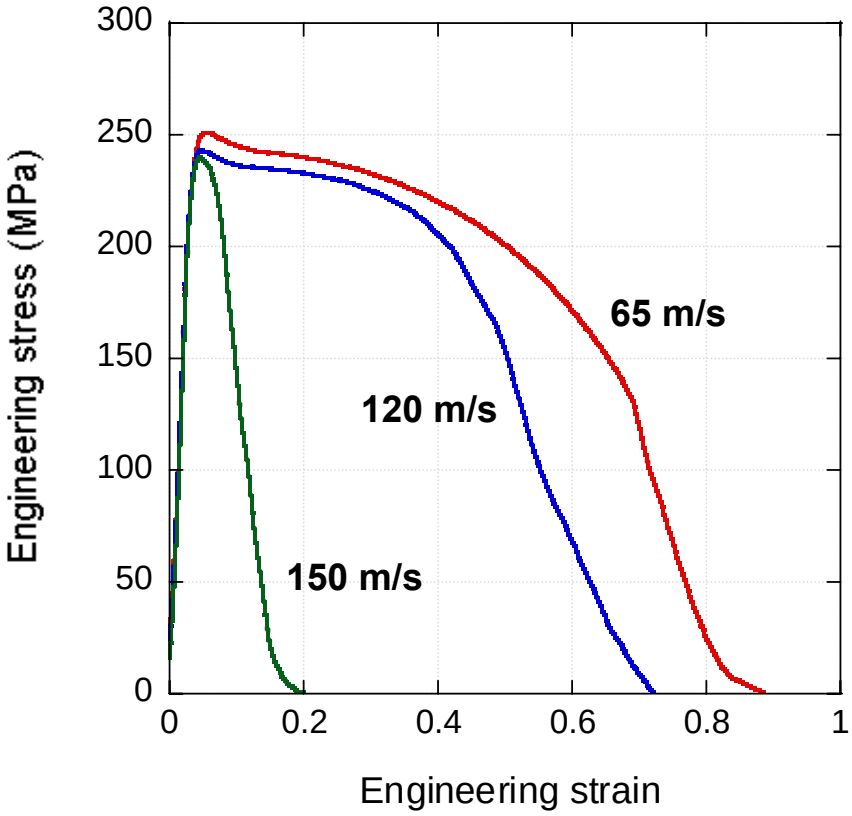


Figure 12. Tensile stress-strain curves for damaged sub-scale specimens

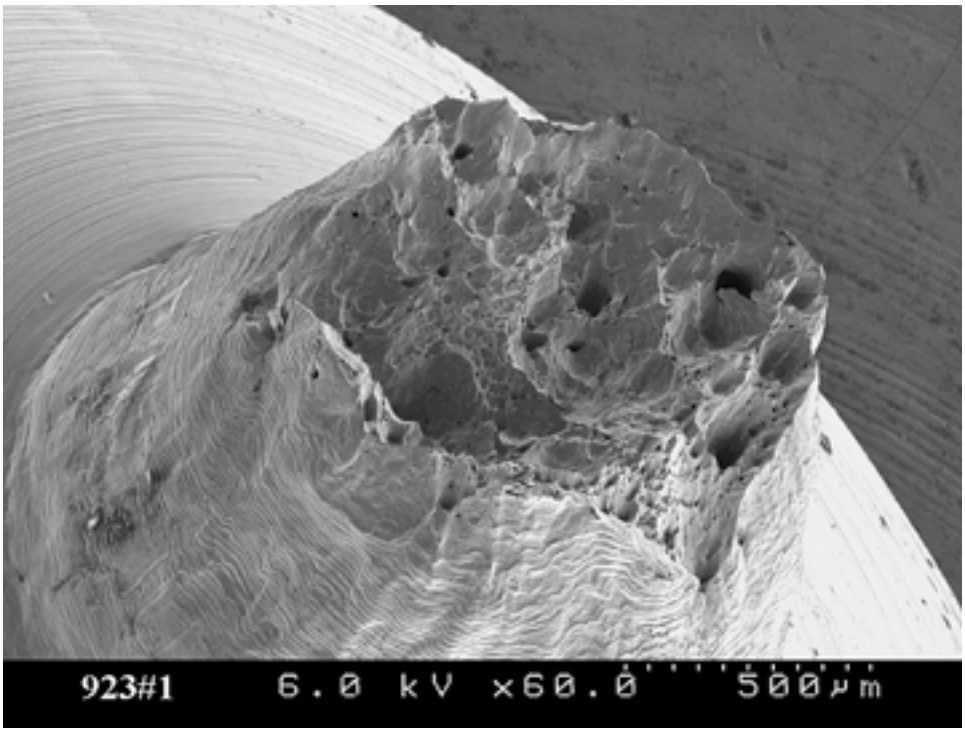


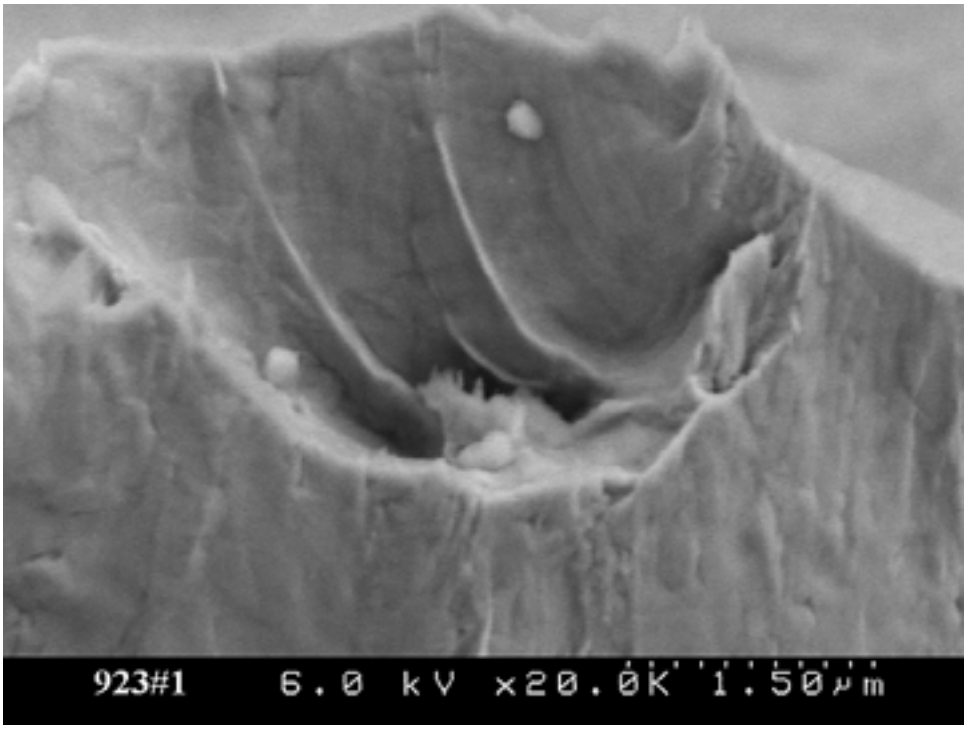


Figure 13. SEM fractography showing dimpled fracture surface and Zirconium containing particles responsible for void formation.

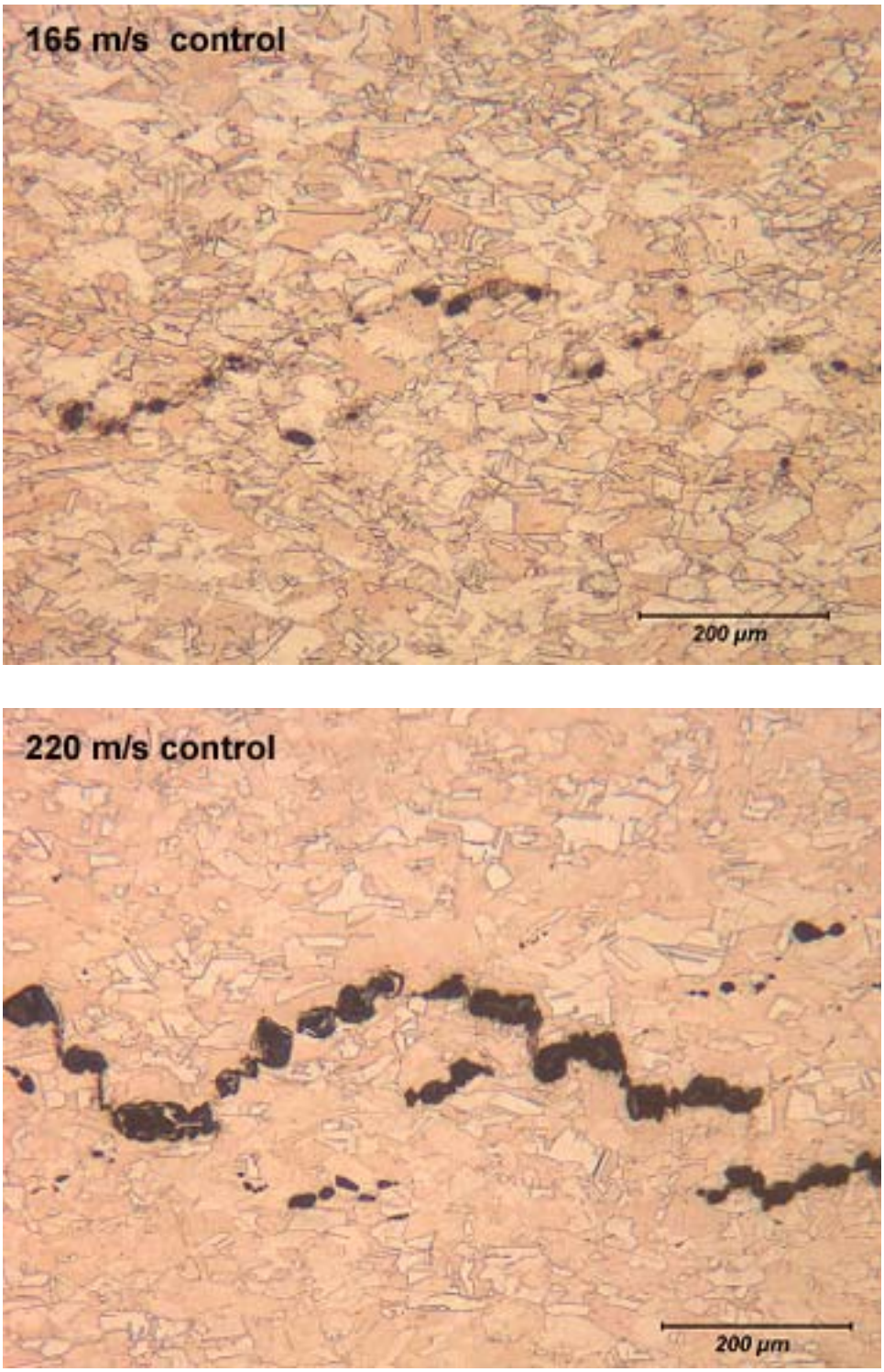


Figure 14. Optical microscopy on as-spalled control specimens for the 165 and 220 m/s recompression tests.

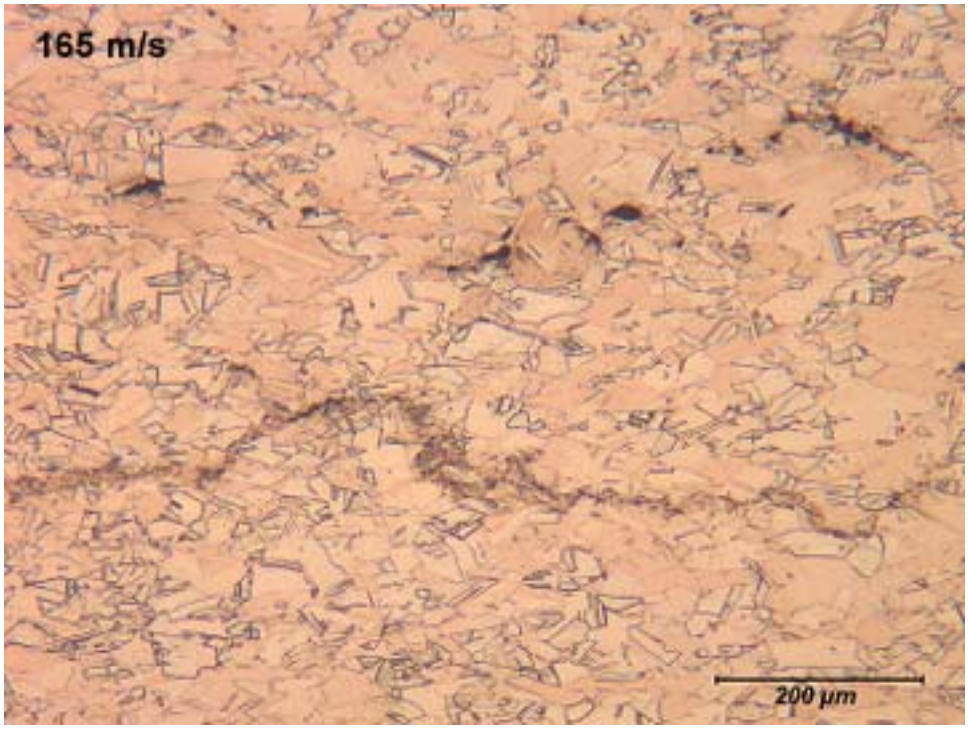


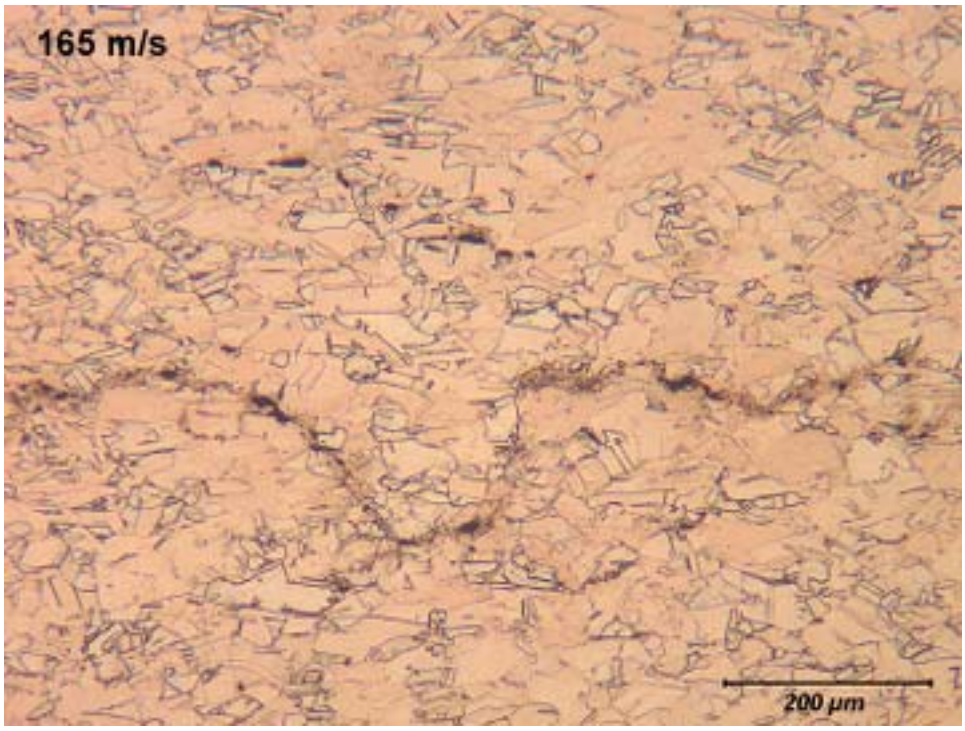


Figure 15. Optical microscopy on specimens spalled and recompressed at 165 m/s.

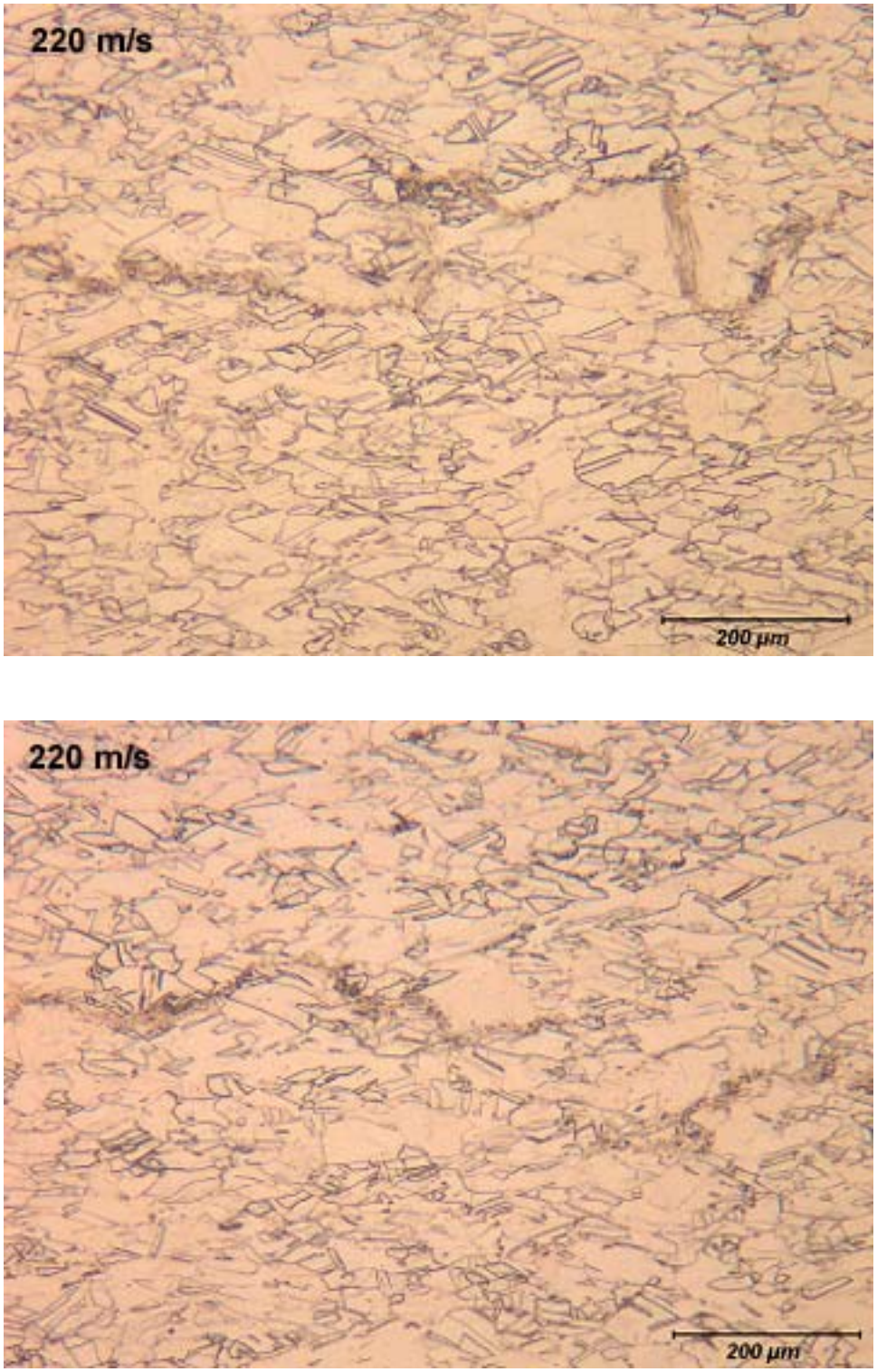


Figure 16. Optical microscopy on specimens spalled and recompressed at 220 m/s.

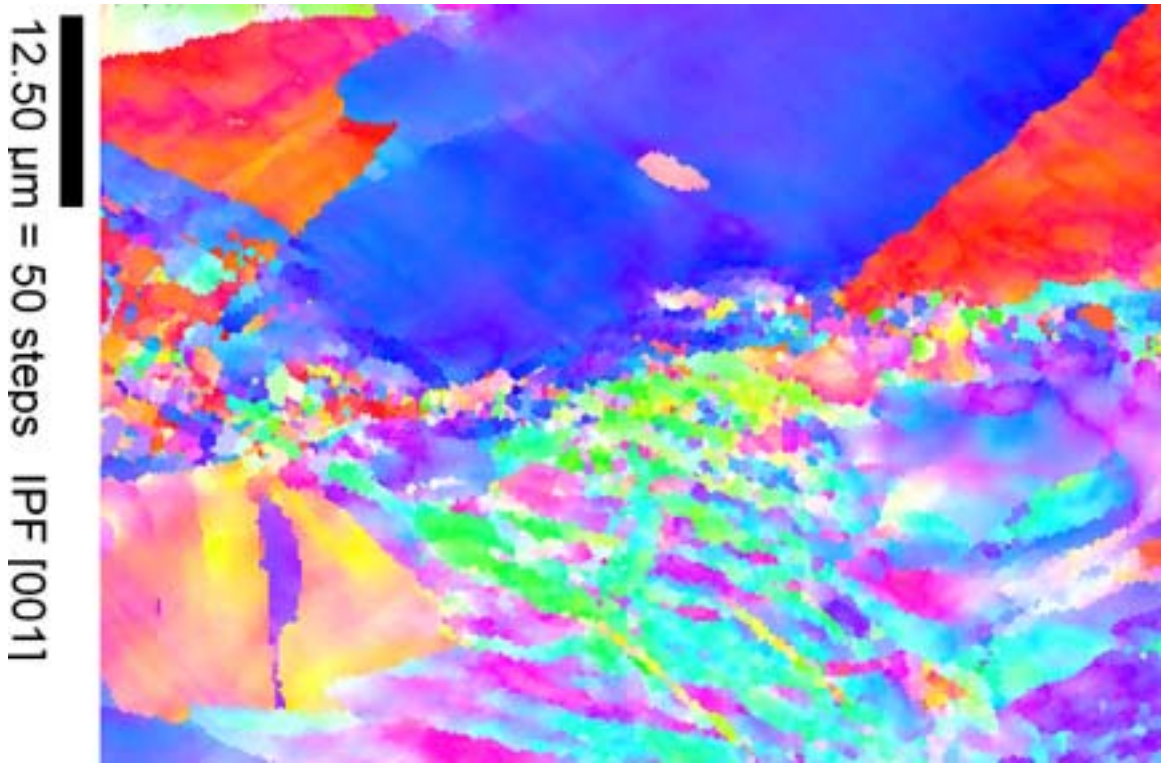


Figure 17. Orientation color map obtained using Electron Backscatter Diffraction. Recompression feature runs horizontally near the center of the image.

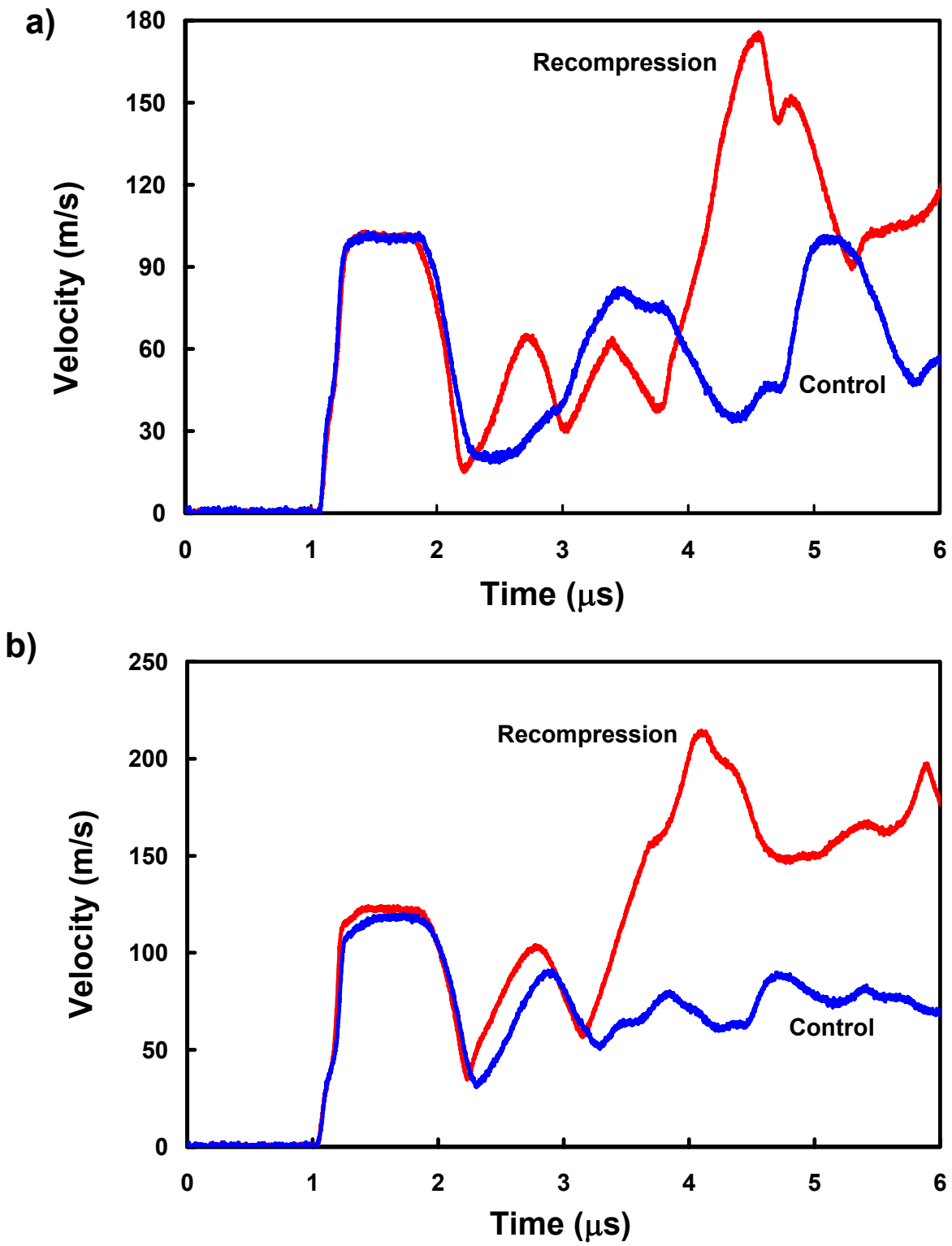


Figure 18. Free surface velocity histories for control and recompression gas gun experiments at a) 165 m/s and b) 220 m/s.

Figure 19. Optical micrograph of recompressed laser spall specimen. The sample was first hit on the right producing a spall blister on the left. The laser was focused on the left for recompression.

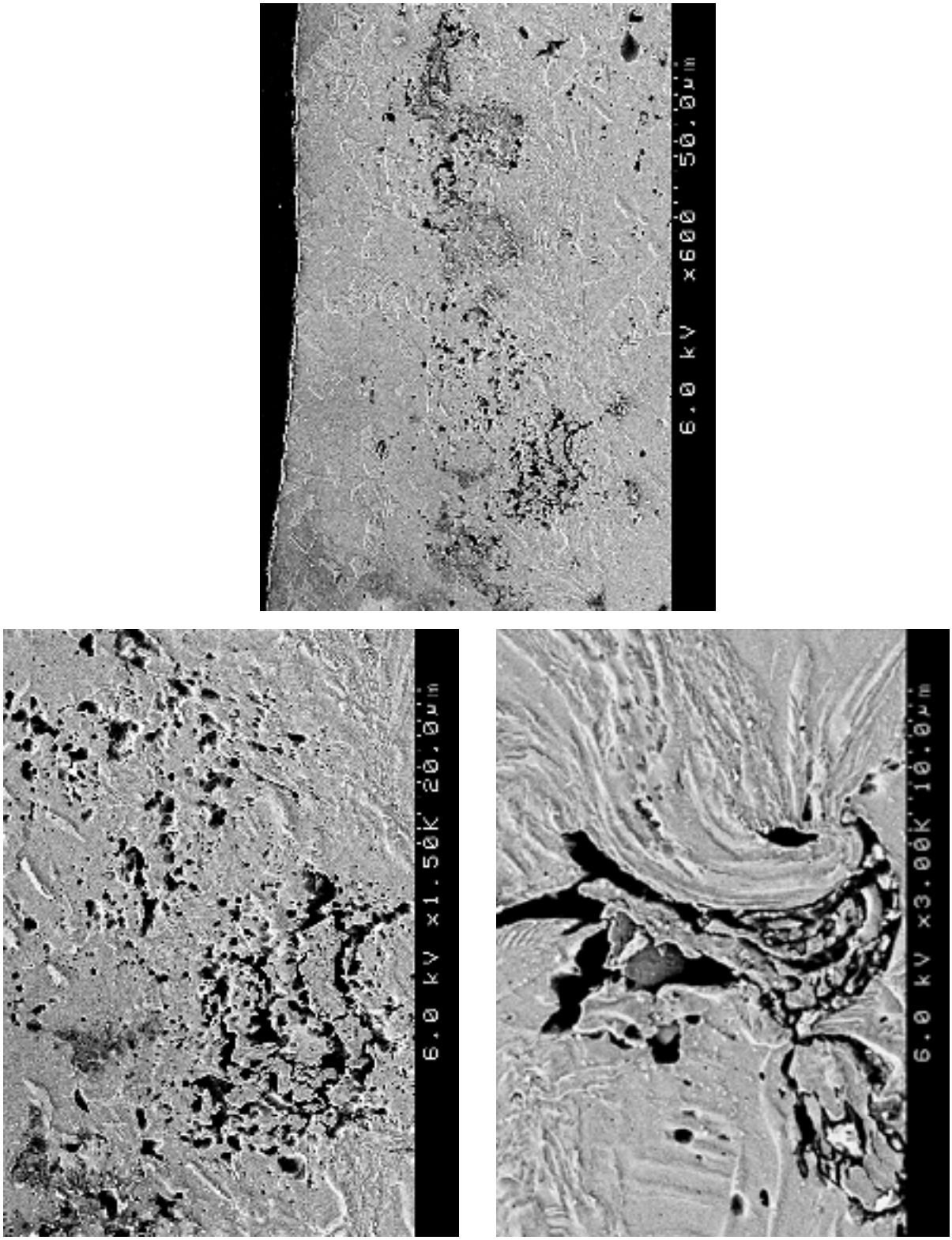


Figure 20. SEM micrographs of laser recompressed copper. The shock traveled left to right.

Figure 22. Laser spall created in 0.5 mm copper specimens for further recompression studies.

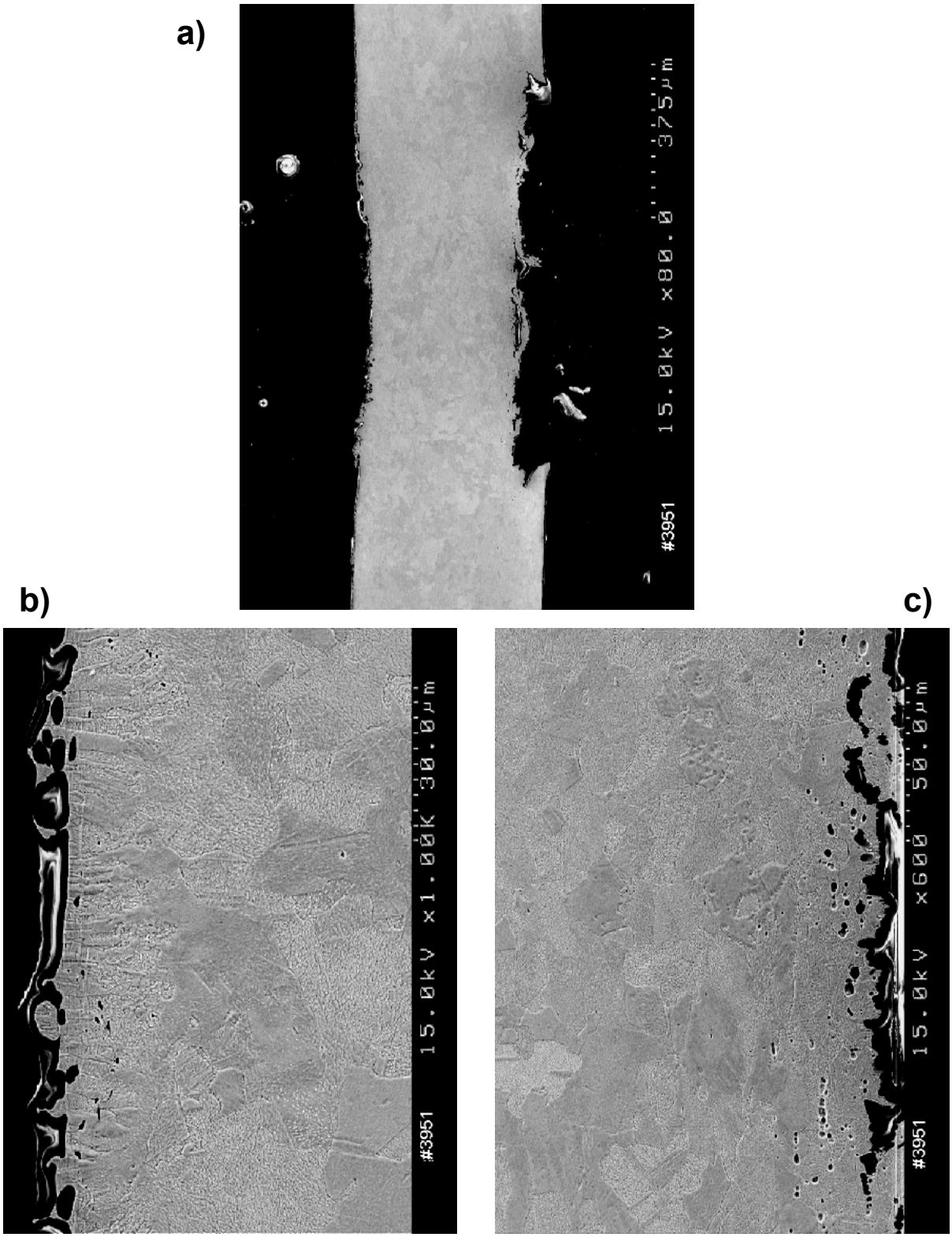


Figure 22. SEM micrographs of laser recompressed spall for the 0.5 mm thick specimens. a) macro view of sample; b) detail of recompressed surface ; c) secondary spall. The recompression shock traveled from left to right.

Figure 23. Unit cell model showing initial void fraction of $10^{-5}$.

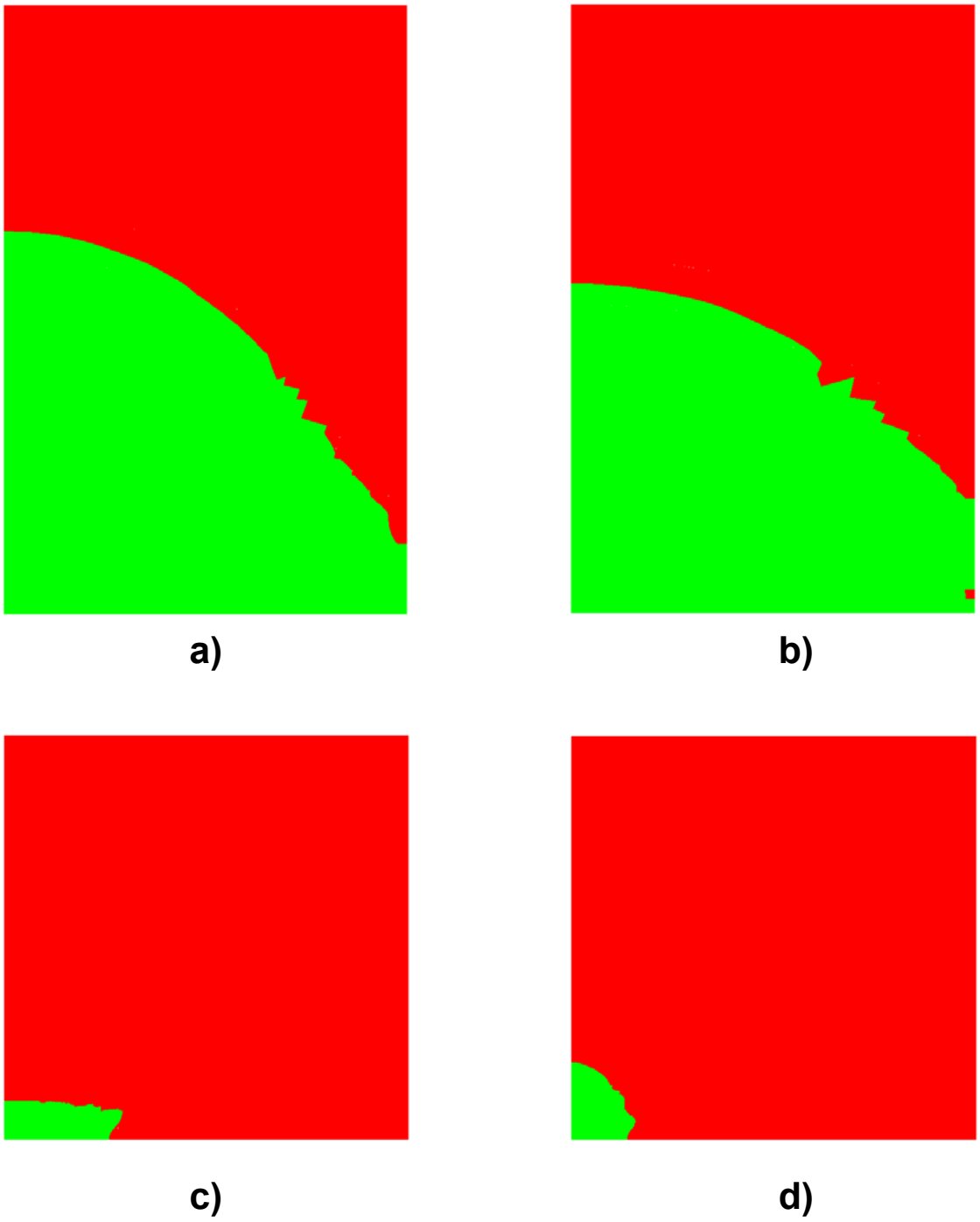


Figure 24. Unit cell models in: a) and b) a fully distended state and c) and d) recompressed to the initial volume. Images on the left have a strain hardening exponent of 0.0001 and images on the right have a strain hardening exponent of 0.2.

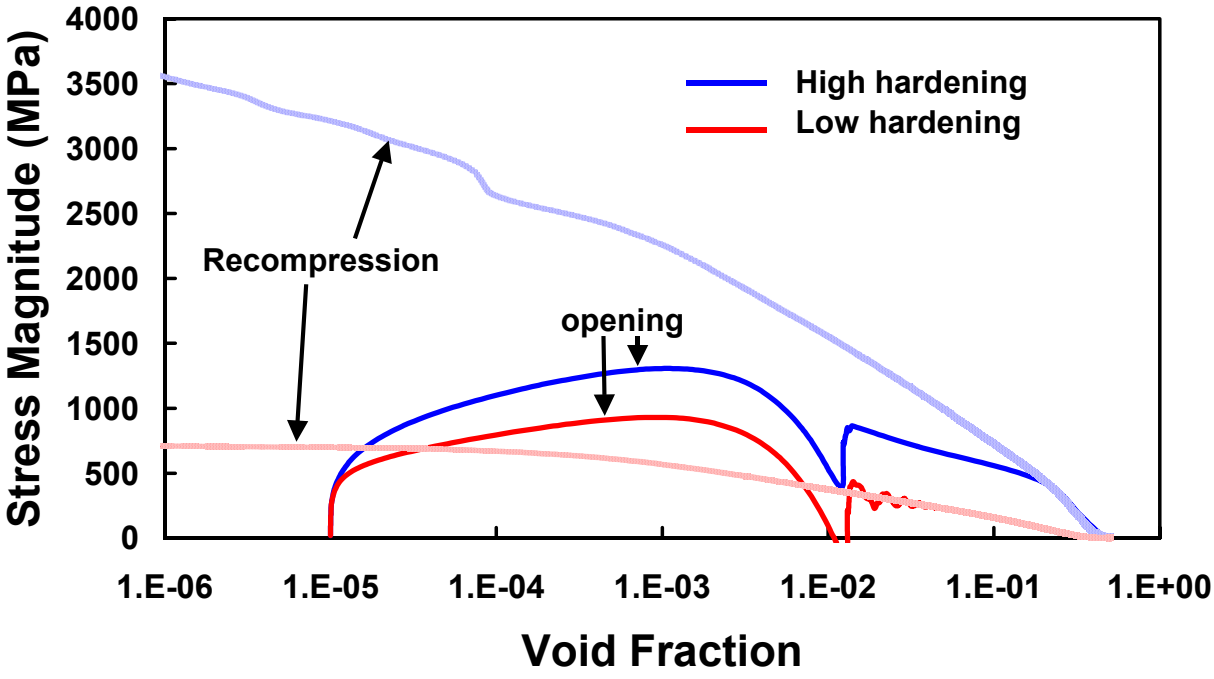


Figure 25. Stress as a function of void fraction for unit cell models deformed in uniaxial strain with high and low strain hardening exponents, 0.2 and 0.0001, respectively.

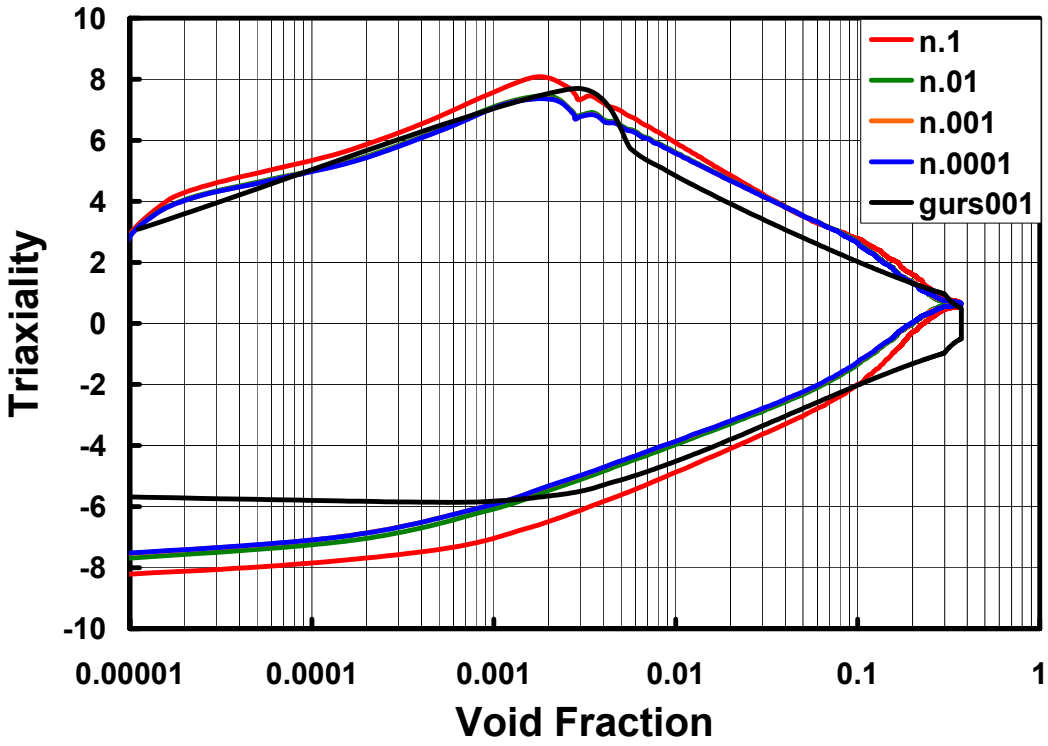


Figure 26. Stress triaxiality (mean stress / von Mises effective stress) as a function of void fraction for uniaxial strain unit cell calculations with a range of hardening exponents. The result from a Gurson model simulation is shown for comparison.